Available online at www.sciencedirect.com

jmr&t
Journal of Materials Research and Technology

journal homepage: www.elsevier.com/locate/jmrt

Original Article

Discovery of new Fe2Ni2CrAlx multi-principal element alloys with promising mechanical properties

Ling Qiao [a,b], *R.V. Ramanujan* [b,**], *Jingchuan Zhu* [a,*]

[a] *School of Material Science and Engineering, Harbin Institute of Technology, Harbin 150001, Heilongjiang, China*
[b] *School of Material Science and Engineering, Nanyang Technological University, 50 Nanyang Avenue, 639798, Singapore*

ARTICLE INFO

Article history:
Received 2 February 2023
Accepted 4 April 2023
Available online 10 April 2023

Keywords:
Microstructure
Mechanical properties
Strengthening mechanism

ABSTRACT

Thermodynamic calculations were utilized to accelerate the pace of discovering promising composition combination by tailoring phase fraction. Then a family of Fe2Ni2CrAlx multi-principal element alloys (MPEAs) were synthesized to investigate the effect of Al on the crystal structure, microstructural evolution, and mechanical properties. A two-phase, face-centered cubic (FCC) and body-centered cubic (BCC), structure was identified in alloys with lower Al content ($x = 0.9$ and 1.1), the alloy consists of structure with stripe patterns. As the Al concentration increased, the FCC phases disappeared, the volume fraction of BCC and B2 phase increased. The morphology turned into polygonal grains in which the periodic maze-shaped microstructure can be identified. Higher Al content dramatically increased the nanohardness and strength of the Fe2Ni2CrAlx MPEAs, but reduced the plasticity. Among the developed alloys, the Fe2Ni2CrAl1.2 alloy displayed the best property combination, with yield stress, compressive strength, and plasticity of 1117.8 MPa, 2961 MPa and 42.3%. These values are superior to most reported as-cast MPEAs. Precipitation strengthening was found to be the main strengthening mechanism responsible for the enhanced mechanical properties of the Fe2Ni2CrAl1.2 alloy. The current work offers the systematic understanding of the strengthening.

1. Introduction

To overcome the restrictions on alloy design and applications, the concept of high entropy alloy (HEAs) or multi-principal element alloys (MPEAs) has been developed, such alloys have been investigated as potential new structural materials for engineering applications [1–3]. With multi-principal elements in the alloys, the alloy tends to form simple solid-solution phases, rather than intermetallic compounds or complex phases [4–6]. Compared with conventional metallic materials, exceptional mechanical properties, e.g., hardness, strength,

---

* Corresponding author.
** Corresponding author.

E-mail addresses: Ramanujan@ntu.edu.sg (R.V. Ramanujan), fgms@hit.edu.cn (J. Zhu).

https://doi.org/10.1016/j.jmrt.2023.04.015

and ductility (at room and high temperatures), corrosion and oxidation resistance, have been reported in previous studies [7–13]. Therefore, alloy design with multi-principal elements has gained immense popularity.

To date, several MPEA systems have been designed and investigated, AlCrCoFeNi [14], AlCrFeNiMo [15], AlCrFeNiMn [16], etc. Particularly taking the cost factor into account, one of the most extensively investigated Co-free alloy systems is the quaternary Al–Cr–Fe–Ni alloy system. To achieve a balance of strength and ductility, more attention has been paid to two-phase or multi-phase MPEAs. Lu et al. [17] have proposed the eutectic alloy idea for MPEAs design. With the aid of this concept, Dong et al. [18] developed an Fe2Ni2CrAl alloy based on the AlCoCrFeNi2 alloy, expensive Co was replaced by cheap Fe. In general, Ni and Co showed a nearly equal partitioning behaviour to FCC and B2 phases. Fe and Cr partition preferably to FCC and BCC phases than the B2 phase. The strength of the alloy is determined by the ratio of Ni to Al as well as by the volume fraction of B2 phase [19,20]. Increasing Fe at the expense of Co will increase the volume fraction of the BCC phase, and increasing the Al-concentration stabilise the B2 phase. With a FCC + BCC two phase structure, the cast Fe2Ni2CrAl alloy showed an excellent combination of high strength and good ductility.

The Fe2Ni2CrAl alloy has attracted extensive scientific interests [21–25]. For instance, Qu et al. [21] proposed that a deep cryogenic treatment can enhance the hardness, yield strength, and wear resistance of this alloy. D. Vogiatzief et al. [23]utilized the processing technique of laser powder bed fusion to prepare this alloy with microstructural refinement as well as further improvement of the mechanical properties. B. Tripathy et al. [25] found that this alloy after thermo-mechanical processing can exhibit enhancement in mechanical properties compared to many reported as-cast materials. Our previous work [26] has utilized the molecular dynamics simulation and finite element method to unveil the compressive behavior of Fe2Ni2CrAl MPEAs. Experiments and molecular dynamics simulation have been performed to uncover its wear mechanism [27]. The results show that the Fe2Ni2CrAl MPEAs show good mechanical properties and wear resistance. While, to further improve the mechanical properties in this alloy system worth further exploration. In general, by adjusting the proportion of alloying elements, the mechanical properties can be enhanced significantly.

To screen the desired alloys in a vast composition space, the trial-and-error experimental method is costly and time-consuming [28,29]. Computational simulations have served as effective tools to aid alloy design for enhancing mechanical properties and providing an in-depth understanding of the deformation and strengthening mechanism [30]. Thermodynamic calculations technique has been applied to clarify the stability and microstructure of HEAs [31–33]. Shu et al. [32] has constructed a pseudo-ternary phase diagram and proposed a CALPHAD aided eutectic high entropy alloy (EHEA) design method to explore more EHEA systems. Huang and Tan et al. [33] used machine learning (ML) and thermodynamic calculations to find the eutectic composition in Ni–Co–Cr–Al system. Two FCC + BCC EHEAs were successfully developed and showed excellent compression strength and high fracture ductility. As potential candidates for possible structural applications, the mechanical property and deformation behavior have attracted extensive attention in the field of MPEAs.

Past research has mainly focused on understanding the microstructure and the properties of the Fe2Ni2CrAl alloy, which consisted of soft FCC and hard BCC phases. To pursue higher mechanical properties, thermodynamic calculations were carried out to accelerate the pace of discovering promising composition combination. Through reasonable composition optimization, we report the microstructure, nanohardness and mechanical properties of Fe2Ni2CrAlx (x is the aluminum content in molar ratio, from 0.9 to 1.3) alloy. The strengthening mechanisms have been discussed in detail with the aim to achieve enhanced mechanical properties. The present work is part of a wide effort to assess the mechanical properties of Fe2Ni2CrAlx based MPEAs at ambient temperatures, which provides insights into developing high-performance MPEAs and understanding the strengthening and deformation mechanism.

2. Methodology

2.1. Materials and experiments

The multi-principal element Fe2Ni2CrAlx alloy system, with different aluminum contents ($x = 0.9$ to 1.3), was produced by arc melting of the high-purity (≥99.9 (at)%) elements under a protective argon atmosphere inside a water-cooled copper cavity. Repeated melting for at least 5 times was carried out to ensure the chemical homogeneity of the alloy. The phase and microstructure of the prepared alloy were investigated using X-ray diffraction (XRD), optical microscopy (OM) and scanning electron microscopy (SEM). The XRD analysis was performed using a XPERT diffractometer with a Cu $K\alpha$ radiation source with 2θ scan from 10° to 110°. SEM investigations were performed utilizing a Zeiss Merlin Compact microscope equipped with an energy-dispersive (EDS) detector which was used for chemical composition measurements. Phase identification and compositional analysis were also carried out by transmission electron microscopy (TEM) and selected area diffraction pattern (SADP) tilt series analysis. Prior to the SEM observation, the extracted sample was mechanically polished using abrasive papers to obtain a flat surface and remove oxides and contamination.

The mechanical properties of the samples were evaluated using nanoindentation and compressive tests. The nanoindentation tests were conducted by using a Nano Indenter G200 (Agilent, US) with a Berkovich indenter under the continuous stiffness measurement (CSM) mode. The testing depth was set as 1200 nm and a constant strain rate of $0.05s^{-1}$ was used in the loading and unloading process. The Poisson's ratio used in this case was 0.3. The compressive tests were performed on an AG-X Plus 250kN/50 kN Electronic Universal Testing Machine. Cylindrical samples of 4 mm in diameter and 6 mm in height were extracted from the ingots for the compressive tests. The compressive tests at room temperature were conducted at an initial loading speed of 0.5 mm/min.

3. Results and discussion

3.1. *CALPHAD calculation results*

To understand the formation of muti-component alloy, phase diagrams play a critical role for the alloy design and processing optimization. On the basics of CALPHAD, Ni based superalloy thermodynamic databases have been successfully employed for the Al–Cr–Fe–Ni alloy system that covers the integral compositional ranges [34]. Considering the solidification and solid state transformation, the equilibrium state of the alloy system can be determined at a given composition and temperature. For Fe2Ni2CrAlx-based MPEAs, the phase formation includes Fe–Cr–Ni forming FCC phase, Fe–Cr forming BCC phase and Ni–Al forming B2 phase. Thus, the phase stability needs to be considered in terms of alloy design.

By using CALPHAD method, Fig. 1 presents the effect of Al and Cr on the volume fraction of B2, BCC and FCC phases in the Fe2Ni2CrAl-based MPEAs. From Fig. 1 (a), the volume fraction of B2 phase increases at first and then decreases with the increasing content of Al. Analysis in Fig. 1 (b) and (c) shows that addition of Al to Fe2Ni2CrAl-based MPEAs stabilizes the BCC phase while destabilizes the FCC solid solution. While, the Cr contributes to the formation of FCC phase in the Fe2Ni2CrAl-based MPEAs. As known, a severe distortion of crystal lattice can be induced by the addition of Al due to the larger atomic radii of Al. The volume fraction of B2 phase dominates the mechanical properties of MPEAs, including the hardness, strength, etc. Combined the calculated results, the content of Al ranging from 17 at.% ~ 21 at.% is tailored for Fe2Ni2CrAl-based MPEAs systems. Accordingly in the following section, Fe2Ni2CrAlx (x = 0.9, 1.1, 1.2, 1.3) alloys are designed for further analysis by experimental characterization and modeling calculations.

3.2. *X-ray diffraction analysis*

Fig. 2 presents the XRD profiles of the as-cast Fe2Ni2CrAlx MPEAs. The phase structure changes with the content of Al element. From Fig. 2 (a), with a lower concentration of Al, the presence of FCC, BCC, and B2 phases can be identified in the Fe2Ni2CrAl0.9 and Fe2Ni2CrAl1.1 alloys. The stronger intensity of the (200) peak indicates a large FCC phase content in the Fe2Ni2CrAl0.9 alloy, this peak becomes weaker when the x value increases to 1.1. For the alloy with higher Al content (x = 1.2 and 1.3), the FCC phases disappear whereas the overlapping peaks of (200) and (211) can be detected in the alloy. Besides, a weak peak intensity of the (100) peak, corresponding to the B2 phase, was identified in Fe2Ni2CrAl1.2 and Fe2Ni2CrAl1.3 alloys. Accordingly, the FCC/BCC + B2 phase structure changes to BCC + B2 phase structure when the Al content increases from x = 0.9 to x = 1.2.

The overlapping peaks of (110) observed in the XRD patterns indicated the formation of a disordered BCC phase and an ordered B2 phase. The Fe2Ni2CrAl1.2 alloy possesses the BCC phase with a lattice parameter of 2.8765 Å. A small fraction of B2 phase with lattice parameter of 2.8782 Å was also observed. The lattice parameters of the two phases are similar and the lattice parameter of the B2 phase is slightly larger than that of the BCC phase. As the volume fraction of Al increases, higher intensity can be observed for the (110) peak of the BCC and B2 crystal structure in the as-cast alloys. The deconvolution method was utilized to estimate the phase fraction. The peak profile fitting on the Fe2Ni2CrAl1.1 alloy (Fig. 2 (b)) show that the phase fraction of BCC and B2 was estimated to be 0.84 and 0.16, respectively. When the x value increases to 1.2, Fig. 2 (c), the volume fraction of the B2 phase increases to 0.28 in the Fe2Ni2CrAl1.2 alloy. Thus, Al plays an important role in enhancing the B2 phase fraction, which agrees well with the evolution trend obtained from CALPHAD calculation.

3.3. *Microstructure*

Fig. 3 presents the metallographic images of Fe2Ni2CrAlx MPEAs obtained from optical microscope. It is observed that the morphology varies with the content of Al. At lower Al content (x = 0.9), coarse phases are identified which delineate the grain boundaries, as plotted in Fig. 3 (a). A fine lamellar microstructure is formed within the grains. From Fig. 3 (b), distinct grain boundaries can be clearly observed and the disordered needle like structure appears near the grain boundary. When the atomic ratio of Al reaches above 1.2, it shows flower-like morphology within the grains, as illustrated in Fig. 3 (c) and (d). With higher Al content (x = 1.3), the needle-like structure completely disappears, as plotted in Fig. 3 (d).

Fig. 4 presents the microstructure of the as-cast Fe2Ni2-CrAlx MPEAs by SEM characterization. At low magnification (Fig. 4 (a) (c) (e) (g)), typical dendrite and inter-dendrite

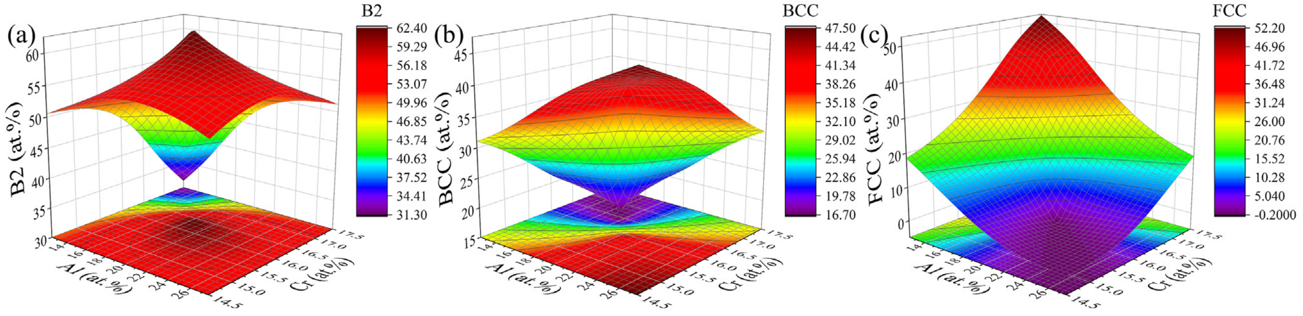

Fig. 1 – The effect of Al and Cr on the volume fraction of phases in the Fe2Ni2CrAl-based MPEAs (a) B2 phase (b) BCC phase (c) FCC phase.

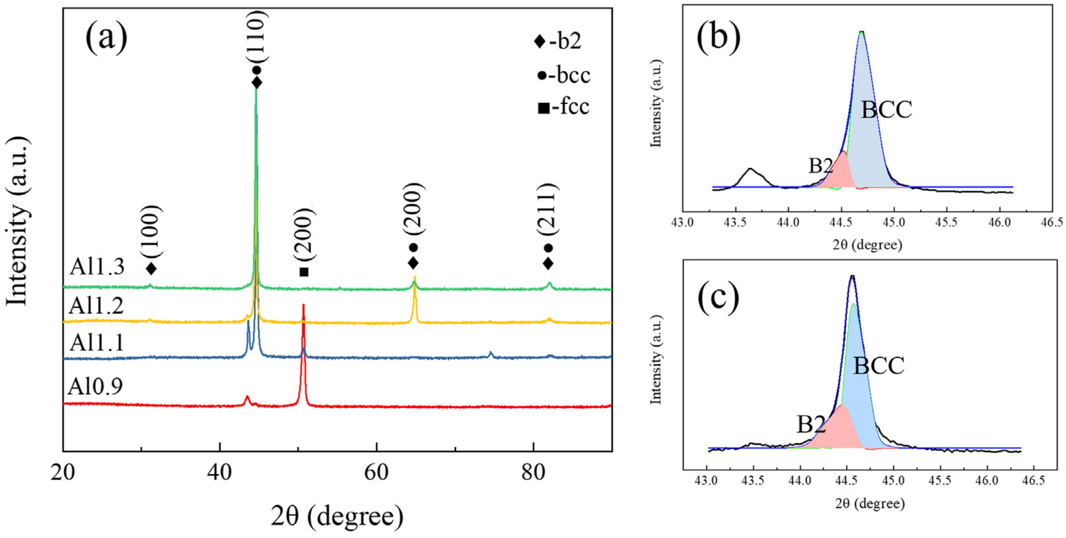

Fig. 2 – (a) XRD patterns of Fe2Ni2CrAlx alloy (x = 0.9, 1.1, 1.2 and 1.3) and profile fitting of (110) on (b) x = 1.1 (c) x = 1.2.

structures were observed in all the samples. Fig. 4 (c) (e) (g) shows distinct grain boundaries and phase separation can be identified within the grains. Fig. 4 (b) (d) (f) (h) show the high-magnification SEM images of each sample. Two regions can be observed, including the interconnected microstructure (region A) and strip microstructure (region B). The periodic maze-shaped microstructure is a typical characteristic of spinodal decomposition in multi-component alloys. The morphology changed with Al concentration. With a small addition of aluminum (x = 0.9), the strip microstructure occupied the higher proportion. As x increased to 1.1, the interconnected microstructures becomes apparent and constructed with BCC/BCC eutectic phases. As can be seen, a large amount of strip structures form and exist in disorder. When x is more than 1.2, the formation of a modulated plate structure is favored due to the spinodal decomposition, which shows good agreement with the higher intensity of the (110) peak of the BCC crystal structure in the XRD analysis. Thus, the Al content

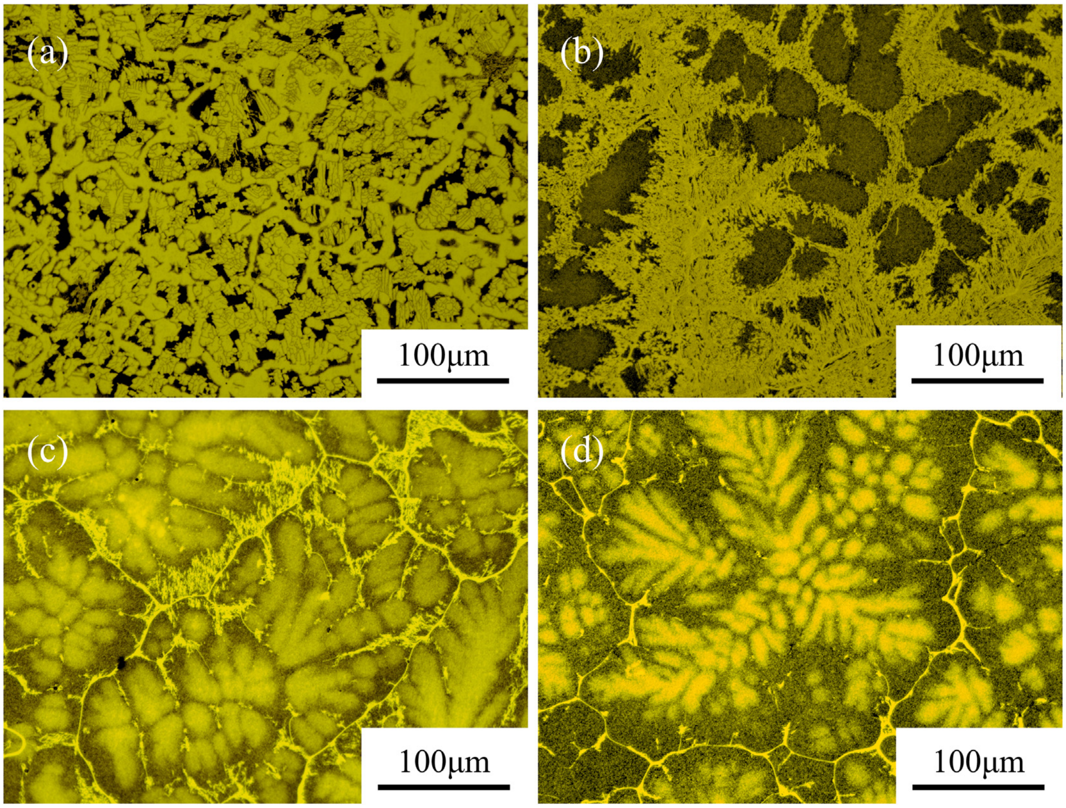

Fig. 3 – Metallographic images of Fe2Ni2CrAlx MPEAs (a) x = 0.9 (b) x = 1.1 (c) x = 1.2 (d) x = 1.3.

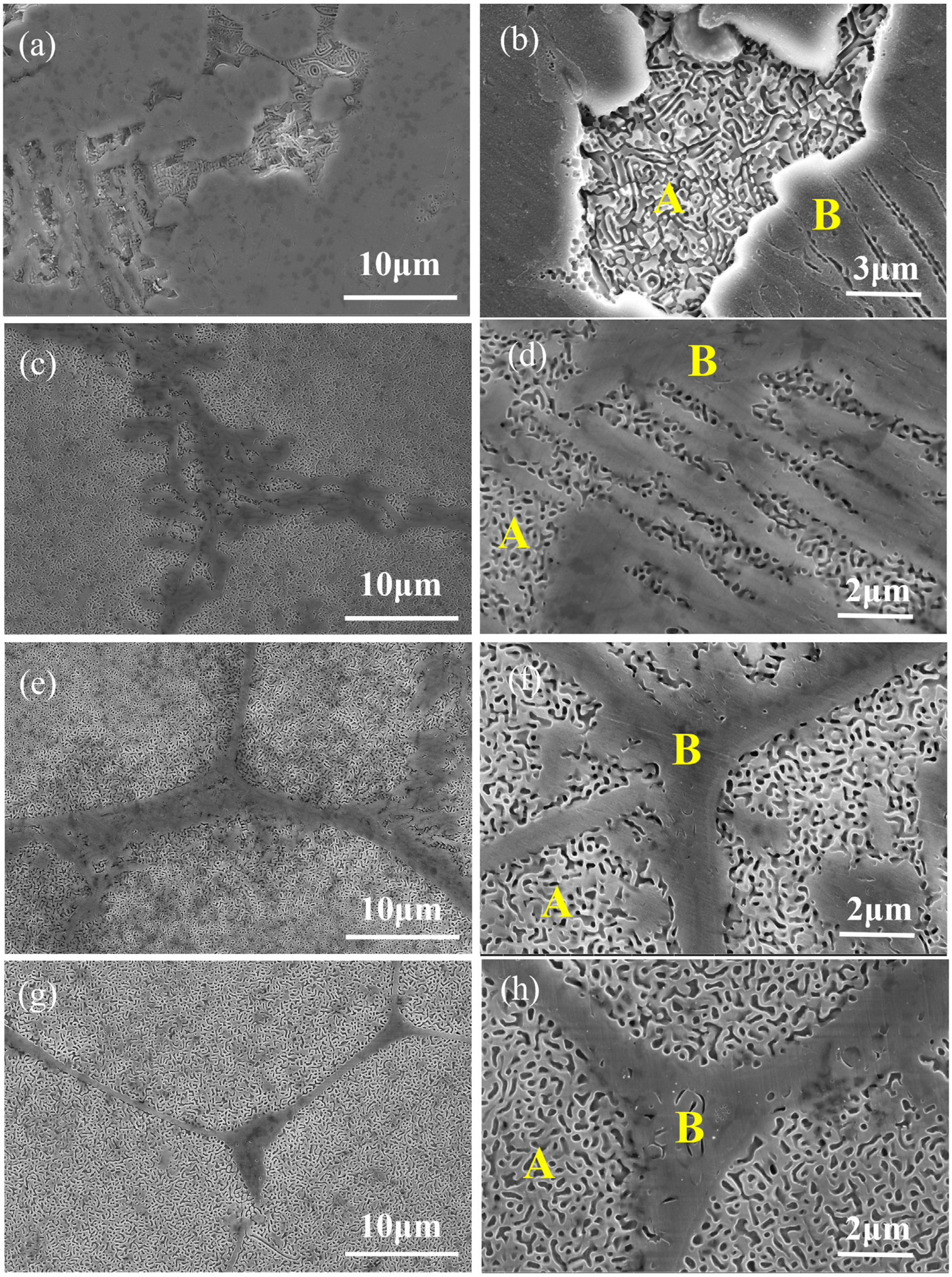

Fig. 4 – Microstructure of Fe2Ni2CrAlx MPEAs.(a) (b) x = 0.9 (c) (d) x = 1.1 (e) (f) x = 1.2 (g) (h) x = 1.3.

has obvious effect on the microstructure, as the Al content increases, the strip morphology turned into polygonal grains and a periodic maze-shaped microstructure in the grains.

Based on the SEM analysis on the microstructure, Table 1 presents the chemical composition of Fe2Ni2CrAlx MPEAs measured for region A and B, which exists significant segregation. At the SEM/EDS level, no obvious defects were detected in the prepared alloy. For the interconnected microstructures in region A, the grains were rich in Ni and Al and Cr and depleted in Fe. Region B consisted of a strip microstructure which was rich in Cr, Fe and depleted in Al, Ni. When the atomic ratio of Al increases to 1.2 and 1.3, the dendritic segregation and interdendritic segregation regions were clearly identified, the dendritic region is Al, Ni rich and the interdendritic region is Cr, Fe rich. Fe and Cr lead to the formation of the BCC phase whereas the presence of Al and Ni contributes to the formation of ordered BCC (B2) phases. Thus, the strip microstructure and grain boundaries correspond to the FCC and Fe–Cr rich BCC phases, the ultrafine interconnected phases mainly consist of B2 phases.

Table 1 – EDS analysis for chemical composition (at.%) of Fe2Ni2CrAlx MPEAs.

Phase	No.	Chemical composition (at.%)			
		Al	Cr	Fe	Ni
Al0.9	Nominal	15.2	16.9	33.8	33.8
	A	20.04	18.64	33.47	27.85
	B	5.15	21.94	44.20	28.71
Al1.1	Nominal	18.0	16.4	32.8	32.8
	A	20.3	17.1	33.6	29.0
	B	16.0	18.3	36.5	29.3
Al1.2	Nominal	19.3	16.1	32.3	32.3
	A	22.9	15.1	28.9	33.1
	B	16.9	20.6	34.4	28.1
Al1.3	Nominal	20.7	15.9	31.8	31.8
	A	20.8	17.9	32.8	28.6
	B	15.6	21.7	35.7	27.0

To further explore the phase structure, Fig. 5 presents a TEM analysis of the as-cast Fe2Ni2CrAl1.2 MPEAs. Fig. 5 (a) and (b) illustrate the typical bright-field micrographs, in which the microstructure is identified with the alternating phases. Fig. 5 (c) and (d) presents the selected-area electron diffraction (SAED) patterns, confirming the existence of a Ni–Al rich ordered B2 phase and a Fe–Cr rich disordered BCC phase. The high-resolution TEM (HRTEM) images of the regions circled by red circles (Fig. 5 (a) and (b)) are displayed in Fig. 5 (e) and (f). The coherent interface between the Ni–Al rich phase and the Fe–Cr rich phase is revealed. The coherent interface can play an important role in the enhancement of mechanical properties by hindering dislocation motion.

Fig. 5(g) presents a typical HAADF (high angular annular dark-field imaging)-STEM (scanning transmission electron microscopy) image, showing the ultrafine structure of the

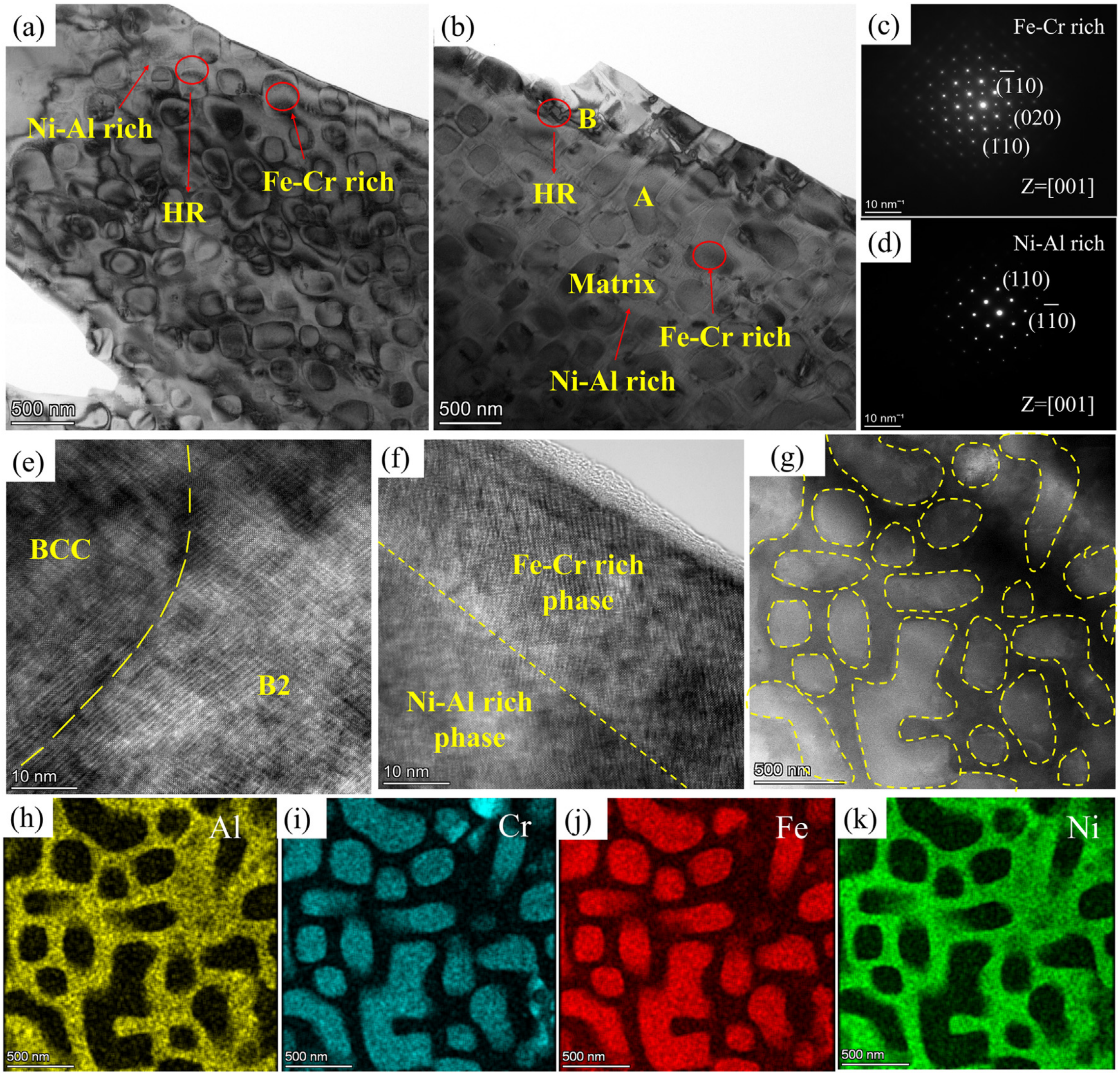

Fig. 5 – TEM analysis results of the Fe2Ni2CrAl1.2 MEAs (a) (b) Bright field image of the microstructure (c) (d) SAED patterns of Fe–Cr rich phase and Ni–Al rich phase (e) (f) HRTEM of the interface between B2 and BCC phases (g)–(k) HAADF images and the elemental distribution.

Table 2 – Chemical composition of each phase in the as-cast Fe2Ni2CrAl1.2 MPEA.

Location	Chemical composition (at.%)			
	Al	Cr	Fe	Ni
A	1.70	18.70	56.58	23.02
B	14.59	4.20	23.67	57.54

Fe2Ni2CrAl1.2 alloy. The irregular spherical precipitates are marked by a filled yellow circle. The EDS mapping results in Fig. 5(h)–(k) demonstrates that the spherical precipitates are enriched with Fe and Cr, and the matrix is enriched with Ni and Al. Based on the different phase structures and morphologies, the EDS point analysis was performed on different locations (marked by A and B) and the chemical composition was summarized in Table 2. The spherical precipitate (location A) primarily comprises of Fe (~56.58 at%) and Cr (~18.70 at %), accompanied by the dissolution of Ni (~23.02 at%). While the matrix phase consists of a large amount of Ni (~57.54 at%) and relatively high concentration of Fe (~23.67 at%) and Al (~14.59 at%), very small concentrations of Cr dissolved in this phase.

3.4. *Nano-indentation test*

As a result of indentation tests, the load–displacement curves of Fe2Ni2CrAlx MPEAs are shown in Fig. 6 (a). A shallower indentation depth is derived with increasing Al concentration, suggesting higher hardness for alloys with relatively high Al content ($x > 1.1$). The average elastic modulus and hardness of each alloy can be derived, Fig. 6(b). For alloys with lower concentration of Al, a high-volume fraction of softer FCC phases can be detected, with hardness values typically between 4.00 and 5.00 GPa. When the x value increases to 1.1, the nanohardness of the alloys increases from 4.45 to 6.47 GPa. With further increase of Al concentration, a significant enhancement to more than 7.00 GPa for the Fe2Ni2CrAl1.2 and Fe2Ni2CrAl1.3 alloys was revealed. As known, the increasing Al content can increase the volume of B2 phases, which possesses higher hardness compared with FCC and BCC phases [35,36], thus increasing the overall hardness of the alloy. Among the developed alloys, the Fe2Ni2CrAl1.2 alloy possesses the highest hardness of 7.45 GPa. In general, this enhancement in nanohardness can be attributed to the increasing volume fraction of the harder BCC phase, as well as the precipitation of nano-sized B2 phases. Solid solution strengthening resulting from the excess Al atoms dissolved in the BCC/FCC phases also contributes to the increased hardness values. Furthermore, the larger atomic radius of Al usually contributes to a severe lattice distortion in MPEAs.

The elastic modulus of Fe2Ni2CrAlx MPEAs exhibits a similar trend with the addition of Al. As the x value increases from 0.9 to 1.2, an evident enhancement can be obtained in the modulus of the alloy, from 177.9 GPa to 222.1 GPa. With

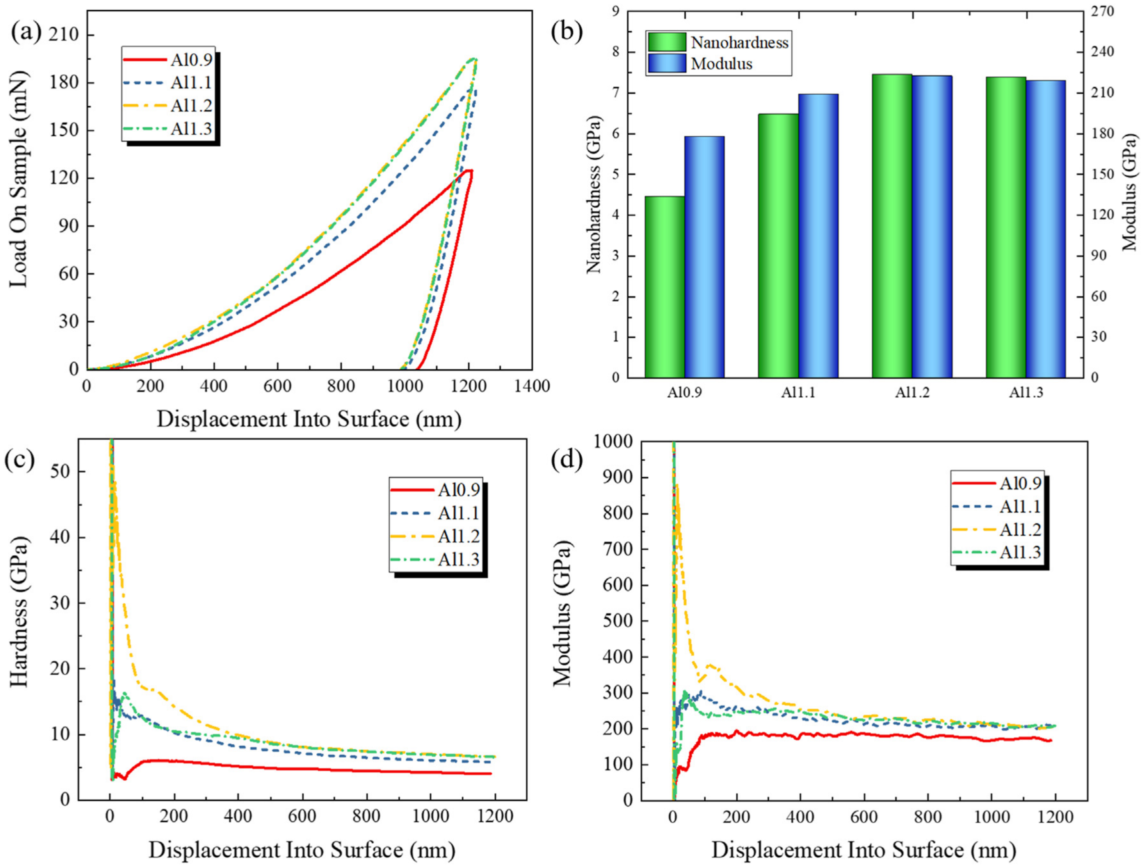

Fig. 6 – (a) The load–displacement (P-h) curves of Fe2Ni2CrAlx MPEAs (b) The average hardness and modulus of the alloys (c) The hardness-indentation depth curves (d) The moludus-indentation depth curves.

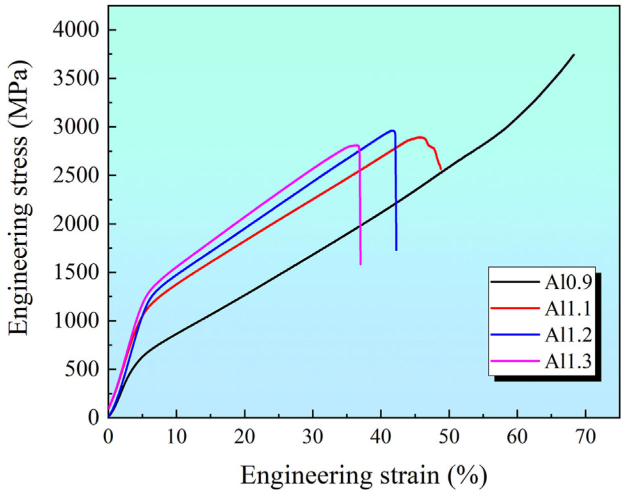

Fig. 7 – Engineering stress–strain curves of the Fe2Ni2CrAlx MPEAs at room temperature.

further increasing Al content (x = 1.3), a slight decrease to 218.7 GPa was observed. Our previous work [27] showed that the modulus of 199.4 GPa can be derived for the Fe2Ni2CrAl alloy. It can be deduced that the developed Fe2Ni2CrAl1.2 alloy shows much higher modulus than Fe2Ni2CrAl alloy.

The Fe2Ni2CrAl1.2 alloy has the highest elastic modulus as well as the highest hardness among the developed alloys. In Fig. 6 (c) and (d), the hardness and modulus values of the developed alloys are plotted against the indentation depth. Similar tendencies can be identified from the curves that the nanohardness reduces with increasing indentation depth. In general, this phenomenon can be attributed to the indentation size effect (ISE), dislocation density usually decreases with the increase of indentation depth.

3.5. *Mechanical properties*

Fig. 7 shows the engineering stress–strain curves of the as-cast Fe2Ni2CrAlx alloy in the compressive condition at room temperature. The strength and plasticity of the alloy are closely associated with Al content. The yield strength and fracture strength can be derived for each sample and are summarized in Table 3. With lower Al concentration, the Fe2Ni2CrAl0.9 alloy exhibits exceptional plasticity since no fracture occurred until the plastic strain of 70% under compression at room temperature. With the addition of Al, it can be observed that the strength of the alloy is dramatically enhanced.

When the x value increases to 1.1, the Fe2Ni2CrAl1.1 alloy has a yield strength of 973.9 MPa, a fracture strength of 2894 MPa, and plastic strain of 48.7%, respectively. It can be deduced that increasing volume fraction of the BCC phase contributes to the enhancement of strength. For alloys with relatively high Al concentration ($x > 1.2$), a further increase from 2894 MPa to 2961 MPa can be observed in the strength of Fe2Ni2CrAl1.2 alloy, with the plastic strain decreasing to 42.3%. With further increase in concentration of Al, the strength of the Fe2Ni2CrAl1.3 alloy decreases to 2811 MPa, accompanied by a reduced plastic strain of 36.9%. From the above analysis, the compressive fracture strength of the as-cast Fe2Ni2CrAl1.2 alloy is the highest among the developed alloys. Tailoring the Al concentration in the Fe2Ni2CrAlx alloy system can tune the mechanical properties of the alloys. The alloy with high FCC phase content exhibits relatively low strength but extended ductility. Enhanced strengthening can be derived via the increasing Al concentration, accompanied by only a small loss of plasticity. Accordingly, the addition of Al contributes to the presence of a desirable microstructure and enhancement in mechanical properties, which was quite attractive for the MPEAs in the as-cast condition.

Table 3 – The mechanical properties of Fe2Ni2CrAlx MEAs at room temperature.

Alloy	Yield strength (MPa)	Fracture strength (MPa)	Plastic strain (%)
Al0.9	484.8	Not fracture	Not fracture
Al1.1	973.9	2894	48.7
Al1.2	1117.8	2961	42.3
Al1.3	1165.9	2811	36.9

From the stress–strain curves, it can be observed that apparent work hardening occurred during deformation. Fig. 8 illustrates the work hardening behavior of the Fe2Ni2CrAlx MPEAs, which is further analyzed by plotting the work hardening rate as a function of true plastic strain. A sharp decline in the strain hardening rate of the Fe2Ni2CrAlx MPEAs after yielding was observed, followed by a slight decrease before fracture.

From Fig. 4, the microstructure of alloys are significantly influenced by the addition of Al, influencing the work-hardening rate during the compression deformation process. The volume fraction of the spinodal structures composed of the BCC and the B2 phases increase with higher concentration of Al, resulting in lower plasticity. As the x value increases from 0.9 to 1.1, an obvious decrease can be observed in the strain hardening rate. With further increase of Al contents (x = 1.2 and 1.3), the strain hardening rate shows a slight increase. Thus, the exceptional plasticity is closely related to the high work-hardening capability.

To further study the work hardening behavior, the Hollomon equation was adopted according to the true stress-true strain data:

$$\sigma = k\epsilon^{n} \tag{1}$$

where k is the strength coefficient and n is the hardening exponent. Taking the logarithmic function on both sides of (1) gives

$$\ln \sigma = \ln k + n\ln \epsilon \tag{2}$$

Fig. 9 presents the relationship of $\ln\epsilon - \ln\sigma$ for the Fe2Ni2CrAlx MPEAs. Table 4 presents the fitting equations for each sample. The work hardening exponent n was determined by using the slopes of curves. The Fe2Ni2CrAl1.2 alloy displays the highest n value of 1.20. In general, the higher n value suggests a good formability. The Fe2Ni2CrAl1.2 alloy possesses a most desirable work hardening ability and is comparable with some conventional metallic materials [37].

To demonstrate the exceptional mechanical properties of Fe2Ni2CrAl1.2 alloy, Fig. 10 provides the plastic strain versus

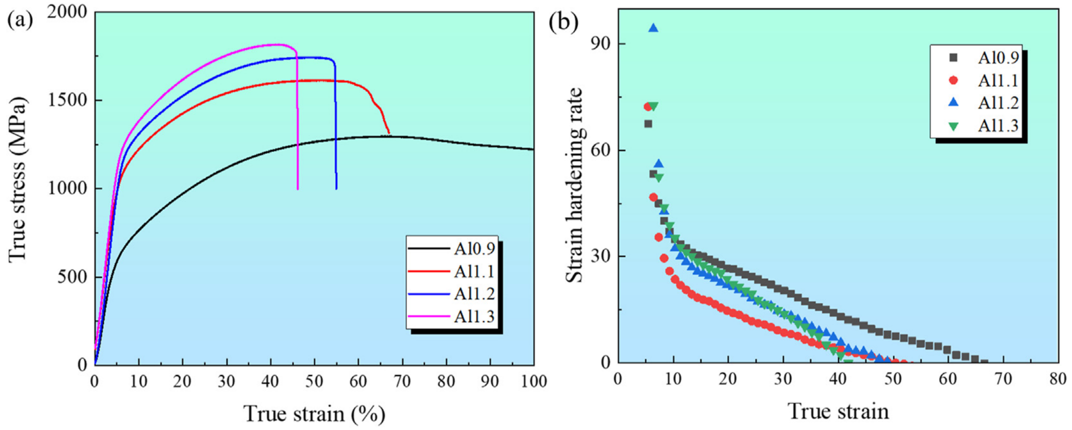

Fig. 8 – The (a) true stress–strain curves and (b) strain hardening rate of Fe2Ni2CrAlx MPEAs.

ultimate compressive strength of several as-cast HEAs for comparison [38–44]. The FCC structure usually possesses good plasticity but low strength, on the other hand, the BCC-type structure presents high strength and poor plasticity. The high compressive strength was attributed to the effect of Al concentration which can tune the volume fraction of the two phases (FCC/BCC). Compared with a Ti-based ultrafine-grain alloy, it is very interesting that the as-cast Fe2Ni2CrAl1.2 alloy has such high strength and plasticity. The FCC phase disappears at Al contents above x = 1.1, due to the combined effect of BCC phases and B2 phases, the mechanical properties of the as-cast Fe2Ni2CrAl1.2 alloy are superior to most of the reported HEAs, even rather than our previously developed Fe2.5Ni2.5CrAl and Fe2Ni2CrAl alloy [28].

As a result, the as-cast Fe2Ni2CrAl1.2 alloy is one of the promising candidates among the reported as-cast HEAs and possesses an excellent combination of strength and plasticity.

3.6. *Strengthening mechanisms of Fe2Ni2CrAl1.2 alloy*

Given the excellent combination of strength and plasticity, the Fe2Ni2CrAl1.2 alloy displays promising mechanical properties among the developed MPEAs. The strengthening mechanisms in the Fe2Ni2CrAl1.2 alloy are now analyzed, and the quantitative contribution of each strengthening mechanism is estimated. Overall, the main strengthening mechanisms that contribute to the compressive yield strength of Fe2Ni2CrAl1.2 alloy can be divided into four independent categories: grain boundary strengthening $\Delta\sigma_{GB}$, dislocation strengthening $\Delta\sigma_{Dis}$, solution strengthening $\Delta\sigma_{SS}$, and precipitation strengthening $\Delta\sigma_p$, respectively [45]. Besides, to examine the misfit effects, the lattice friction strength of the alloy was also considered. Then the total yield stress can be expressed as Eq. (3).

$$\sigma_y = \sigma_i + \Delta\sigma_{GB} + \Delta\sigma_{Dis} + \Delta\sigma_{SS} + \Delta\sigma_p \tag{3}$$

where σ_i is the intrinsic strength caused by lattice resistance which is composed of all the alloying elements. The lattice friction stress was assumed to be 108.04 MPa according to the mixing rule [46]. The contribution of the different kinds of strengthening mechanism is discussed in detail.

3.6.1. *Grain boundary strengthening*

The grain boundary strengthening is a typical strengthening mechanism in the metallic materials, which can hinder dislocation movement and further improve the strength. The contributions of grain boundary strengthening can be estimated via the Hall–Petch relationship, as

$$\Delta\sigma_{GB} = K_{HP} d^{-1/2} \tag{4}$$

where K denotes the constant of strengthening coefficient and d is the average grain size. According to the [46], the K value of Fe2Ni2CrAl1.2 alloy can be estimated as 0.3854 MPa $\cdot\, m^{1/2}$. The average value of d can be estimated from the optical micrograph (Fig. 4) as ~ 50 μm: the contribution of grain refined strengthening is about 60.9 MPa.

3.6.2. *Dislocation strengthening*

The contribution of dislocation strengthening can be derived using the well-known Eq. (5).

$$\Delta\sigma_{Dis} = M\alpha Gb\rho^{1/2} \tag{5}$$

where, M is the Taylor factor with a value of 2.73 for bcc structure [47], α is a constant of 0.4. G denotes the shear modulus, which can be obtained according to $G = E/2(1+\nu)$, and ρ is Poisson ratio equals to 0.3 for the bcc HEAs. According to the elastic modulus measured by nano-indentation experiment, the G of Fe2Ni2CrAl1.2 can be assumed as 144.4 GPa. Besides, b is the Burgers vector, which can be obtained by $b = \sqrt{3}a/2 = 0.248\text{nm}$ [48], ρ represents the density of dislocation and can be derived by Eq. (6) [49].

$$\rho = 2\sqrt{3}\epsilon/db \tag{6}$$

where, ϵ is the lattice strain, d is the average grain size. Then the dislocation density can be determined as $1.12 \times 10^{12} m^{-2}$, suggesting high dislocation densities. Thus, the strength increasing from dislocation can be estimated to be 41.4 MPa.

3.6.3. *Solid solution strengthening*

The contribution of solution strengthening can be estimated via the model proposed by Gypen and Deruyttere, which can be expressed as [50].

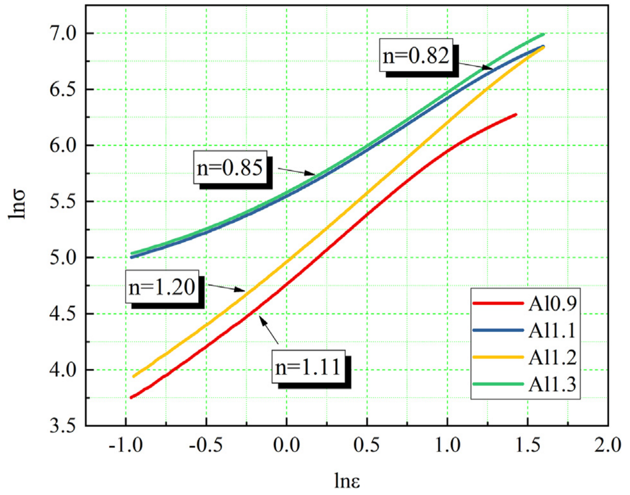

Fig. 9 – The $\ln\epsilon - \ln\sigma$ relationship of Fe2Ni2CrAlx MPEAs.

Table 4 – The fitting equations for each sample.

Alloy	Fitting equation
Al0.9	$\ln\sigma = 1.11\ln\epsilon + 4.8$
Al1.1	$\ln\sigma = 0.82\ln\epsilon + 5.6$
Al1.2	$\ln\sigma = 1.20\ln\epsilon + 5.0$
Al1.3	$\ln\sigma = 0.85\ln\epsilon + 5.6$

$$\Delta\sigma_{SS} = \left(\Sigma_i \left(k_i \cdot \sqrt{C_i}\right)^{1/p}\right)^p \tag{7}$$

where k_i is the strengthening coefficient, C_i is the atomic percentage of solute i. p is a constant equal to 1/2. With respect to the Fe2Ni2CrAl1.2 alloy, it exhibits very small difference in the atomic size of Cr, Fe, and Ni elements. Recognising this, the element Al, which possesses the largest atomic radius among the 4 principal elements, can be considered as the major solute in the solvent matrix. The k_i value of Al element is 225 MPa/(at. %) thus the $\Delta\sigma_{SS}$ can be estimated to be 107.9 MPa.

3.6.4. *Precipitation strengthening*

Due to the spinodal decomposition in Fe2Ni2CrAl1.2 alloy, one should pay particular attention to the second phase strengthening effect, especially spinodal decomposition hardening. The second phase hardening mechanisms primarily includes Orowan-type and precipitate shearing. The shearing mechanism dominates in this case with coherent and small precipitates. Considering the effect of precipitates sheared by dislocations, three contribution factors should be considered: the coherency strengthening ($\Delta\sigma_{CS}$) mechanism, the modulus strengthening ($\Delta\sigma_{MS}$) mechanism and the order strengthening ($\Delta\sigma_{OS}$) mechanism. The equations available to quantitatively calculate the strength increments can be expressed as Eqs. 8–10 [51].

$$\Delta\sigma_{CS} = M\alpha_\epsilon (G\epsilon_a)^{3/2}\left(\frac{rf}{0.5Gb}\right)^{1/2} \tag{8}$$

$$\Delta\sigma_{MS} = M \times 0.0055 \times (\Delta G)^{3/2}\left(\frac{f}{G}\right)^{1/2}\left(\frac{r}{b}\right)^{\frac{3m}{2}-1} \tag{9}$$

$$\Delta\sigma_{OS} = M \times 0.81 \times \frac{\gamma_{apb}}{2b}\left(\frac{3\pi f}{8}\right)^{1/2} \tag{10}$$

where α_ϵ is a constant equal to 2.6, ϵ is the constrained lattice misfit $\epsilon_c = 2\epsilon/3$, ΔG is the shear modulus mismatch between precipitates and matrix, f is the volume fraction of the precipitates, r is the average radius of the precipitates, m is a

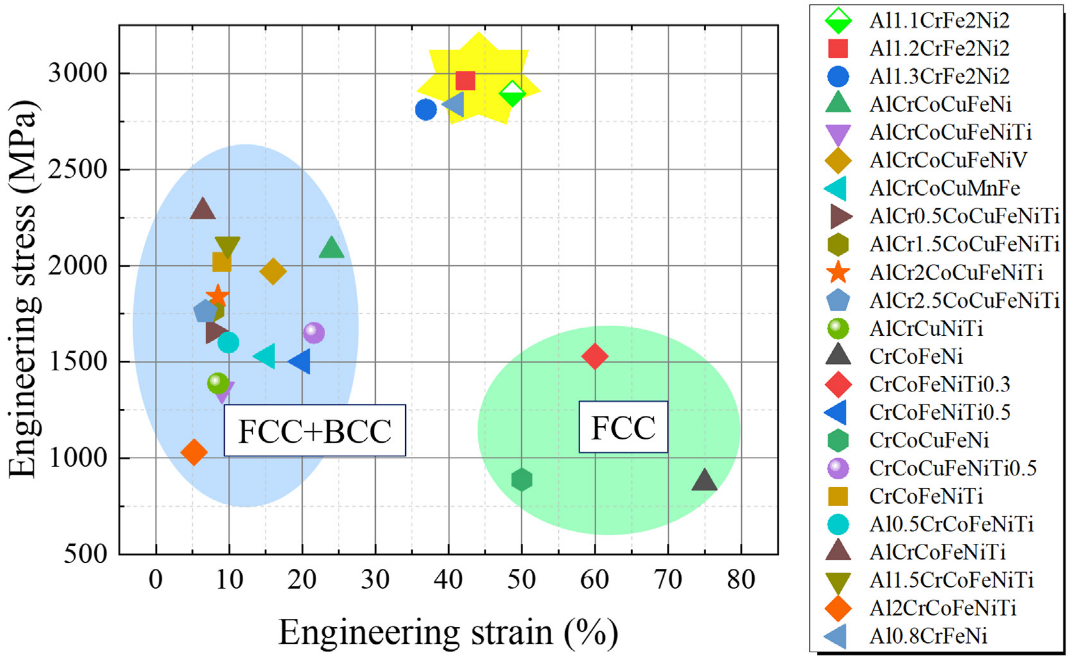

Fig. 10 – The mechanical properties of Fe2Ni2CrAlx alloy compared with other reported HEAs [38–44].

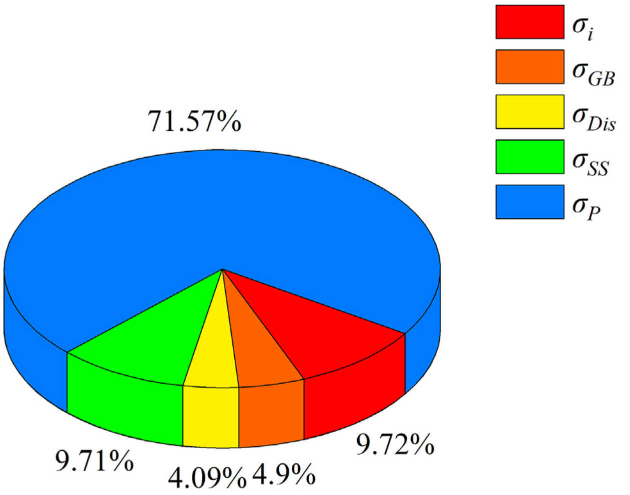

Fig. 11 – The contribution of each strengthening mechanism.

constant with the value of 0.85, γ_{apb} is the anti-phase boundary energy of the precipitates, 0.25J/m^2. The value of ϵ can be estimated from XRD patterns by Williamson-Hall method [52] and the value of r can be measured by TEM images. Accordingly, the strength increments caused by the precipitation BCC nanoparticles are evaluated to be 829.2 MPa.

3.6.5. *Total strengthening*

As mentioned above, the total strength increment could be deduced as 1141.04 MPa. It is in excellent agreement with the yield strength ($\sigma = 1117.8$ MPa) from experiment. The contribution of each strengthening mechanism is displayed in Fig. 11. To conclude, the precipitation strengthening plays a predominant role among the strengthening mechanisms.

4. Conclusion

In this work, thermodynamic calculations were applied to multi-component alloy design by tailoring phase fraction. A new class of Co-free Fe2Ni2CrAlx MPEAs were designed and prepared which possesses exceptional mechanical properties. Detailed microstructural characterization was carried out by means of XRD, SEM, and TEM techniques, as well as mechanical properties performed by nano-indentation tests and compressive tests. The main conclusions are.

(1) The phase and microstructure of this Fe2Ni2CrAlx alloy can be tuned by the Al concentration. The presence of FCC, BCC and B2 phase were identified in the alloy with lower Al content (x = 0.9 and 1.1). As the Al concentration increased (x > 1.1), the volume fraction of the B2 phase increases and the FCC phase disappears. The strip morphology turned into polygonal grains and a periodic maze-shaped microstructure can be identified in the grains. The EDS results show that the dendritic segregation is Al–Ni rich and interdendritic segregation is Fe–Cr rich.

(2) The irregular spherical precipitates identified in the FeNiCrAl1.2 alloy by TEM analysis are enriched in Fe and Cr. An ultra-fine spinodal decomposition microstructure of the BCC and B2 phases can be observed with coherent interfaces.

(3) Higher Al content increased the nanohardness and elastic modulus of the alloys. The Fe2Ni2CrAl1.2 alloy possesses the highest hardness and elastic modulus of 7.45 GPa and 222.1 GPa. The enhancement in nanohardness can be attributed to the increasing volume fraction of the harder B2 phase.

(4) The fracture strength increases dramatically from 484.4 MPa to 1165.9 MPa with the increasing concentration of Al (x value from 0.9 to 1.3). The as-cast Fe2Ni2CrAl1.2 alloy displayed the most desirable combination of strength and plasticity with an engineering plastic strain of 42.3%, the yield strength of about 1117.8 MPa and a high fracture strength of about 2961 MPa under uniaxial compression at room temperature. The mechanical properties of the Fe2Ni2CrAl1.2 alloy are superior to those of most reported as-cast HEAs at room temperature.

(5) The strengthening mechanisms of the Fe2Ni2CrAl1.2 alloy were discussed. The contributions of strengthening mechanisms were quantitatively estimated which was in excellent agreement with the experimental value. The results show that the precipitation strengthening mechanism plays a significant role in enhancing the mechanical properties.

Data availability statement

The raw/processed data required to reproduce these findings cannot be shared at this time as the data also forms part of an ongoing study.

Declaration of Competing Interest

The authors declare that they have no known competing financial interests or personal relationships that could have appeared to influence the work reported in this paper.

Acknowledgements

This work is supported by AME Programmatic Fund by the Agency for Science, Technology and Research, Singapore under Grants No. A1898b0043 and A18B1b0061 and the China Scholarship Council.

REFERENCES

[1] Yeh JW. Alloy design strategies and future trends in high-entropy alloys. JOM 2013;35(12):1759–71.
[2] Yeh JW, Chen SK, Lin SJ, Gan JY, Chin TS, Shun TT, et al. Nanostructured high-entropy alloys with multiprincipal

elements-novel alloy design concepts and outcomes. Adv Eng Mater 2004;6:299–303.

[3] Wang L, Zhang F, Nie Z, Wang L, Wang F, Wang B, et al. Abundant polymorphic transitions in the Al0.6CoCrFeNi high-entropy alloy. Materials Today Physics 2019;8:1–9.

[4] Zhang W, Liaw PK, Zhang Y. Science and technology in high-entropy alloys. Science China Materials 2018;61(1):2–22.

[5] Zhang Yong, Zuo Ting Ting, Tang Zhi, Gao Michael C, Dahmen Karin A, Liaw Peter K, et al. Microstructures and properties of high-entropy alloys. Prog Mater Sci 2014;61:1–93.

[6] Qiao Ling, Liu Yong, Zhu Jingchuan. A focused review on machine learning aided high-throughput methods in high entropy alloy. J Alloys Compd 2021;877:160295.

[7] Zhang L, Zhang Y. Tensile properties and impact toughness of $AlCo_xCrFeNi_{3.1-x}(x = 0.4, 1)$ high-entropy alloys. Frontiers in Materials 2020;7:92.

[8] Li Ruixuan, Zheng Ren, Wu Yuan, He Zhanbing, Liaw Peter K, Ren Jingli, et al. Mechanical behaviors and precipitation transformation of the lightweight high-Zn-content Al-Zn-Li-Mg-Cu alloy. Mater Sci Eng, A 2021;802:140637.

[9] Yan Xuehui, Zhang Yong. A body-centered cubic Zr50Ti35Nb15 medium-entropy alloy with unique properties. Scripta Mater 2020;178:329–33.

[10] Qiao Ling, Bao Aorigele, Lai Zhonghong, Liu Yong, Zhu Jingchuan, Wang Yuan. Alloy design and properties optimization of multi-component alloy based on solidification characteristics. Mater Sci Eng, A 2020:140576.

[11] Kim Young-Kyun, Joo Yeun-Ah, Kim Hyoung Seop, Lee Kee-Ahn. High temperature oxidation behavior of Cr-Mn-Fe-Co-Ni high entropy alloy. Intermetallics 2018;98:45–53.

[12] Cao BX, Wei DX, Zhang XF, Kong HJ, Zhao YL, Hou JX, et al. Intermediate temperature embrittlement in a precipitation-hardened high-entropy alloy: the role of heterogeneous strain distribution and environmentally assisted intergranular damage. Materials Today Physics 2022;24:100653.

[13] Cai Jianfeng, Yang Junxuan, Liu Guoqiang, Wang Hongxiang, Shi Fanfan, Tan Xiaojian, et al. Ultralow thermal conductivity and improved ZT of CuInTe2 by high-entropy structure design. Materials Today Physics 2021;18:100394.

[14] Zhao Yuqiao, Cui Hongzhi, Wang Mingliang, Zhao Yong, Zhang Xue, Wang Canming. The microstructures and properties changes induced by Al:Co ratios of the AlXCrCo2-XFeNi high entropy alloys. Mater Sci Eng, A 2018;733:153–63.

[15] Munitz A, Edry I, Brosh E, Derimow N, MacDonald BE, Lavernia EJ, et al. Liquid phase separation in AlCrFeNiMo0.3 high-entropy alloy. Intermetallics 2019;112:106517.

[16] Nong Zhi-Sheng, Lei Yu-Nong, Zhu Jing-Chuan. Wear and oxidation resistances of AlCrFeNiTi-based high entropy alloys. Intermetallics 2018;101:144–51.

[17] Lu YP, Dong Y, Guo S, Jiang L, Kang HJ, Wang TM, et al. Sci Rep 2014;4:6200.

[18] Dong Yong, Gao Xiaoxia, Lu Yiping, Wang Tongmin, Li Tingju. A multi-component AlCrFe2Ni2 alloy with excellent mechanical properties. Mater Lett 2016;169:62–4.

[19] Joseph J, Imran M, Hodgson PD, Barnett MR, Fabijanic DM. Towards the large-scale production and strength prediction of near-eutectic AlxCoCrFeNi2.1 alloys by additive manufacturing. Manufacturing Letters 2020;25:16–20.

[20] Tian QW, Zhang GJ, Yin KX, Cheng WL, Wang YN, Huang JC. Effect of Ni content on the phase formation, tensile properties and deformation mechanisms of the Ni-rich AlCoCrFeNix (x=2, 3, 4) high entropy alloys. Mater Char 2021;176:111148.

[21] Li Chengze, Qu Yingdong, Zhang Yufeng, Lv Qingyao, Qi Hao. Effect of deep cryogenic treatment on the microstructure and mechanical properties of AlCrFe2Ni2 High-entropy alloy. Mater Res Express 2020;7:036504.

[22] Wei C, Du X, Lu Y, Jiang H, Li T, Wang T. Novel as-cast AlCrFe2Ni2Ti05 high-entropy alloy with excellent mechanical properties. Int J Miner Metall Mater 2020;27:1312–7.

[23] Dimitrios Vogiatzief, Alper Evirgen, Sergej Gein, Rocio Molina Veronica, Andreas Weisheit, Pedersen Mikkel. Laser powder bed fusion and heat treatment of an AlCrFe2Ni2 high entropy alloy. Frontiers in Materials 2020;7:248.

[24] Liu Xiaotao, Ding Hua, Huang Yi, Xiao Bai, Zhang Qian, Zhang Haitao, et al. Evidence for a phase transition in an AlCrFe2Ni2 high entropy alloy processed by high-pressure torsion. J Alloys Compd 2021;867:159063.

[25] Tripathy B, Malladi SRK, Bhattacharjee PP. Development of ultrafine grained cobalt-free AlCrFe2Ni2 high entropy alloy with superior mechanical properties by thermo-mechanical processing. Mater Sci Eng, A 2022;831:142190.

[26] Qiao Ling, Zhu Jingchuan. Unveiling the compressive behavior of Fe2Ni2CrAl high entropy alloy: a combined molecular dynamics and finite element study. Mater Today Commun 2023;34:105296.

[27] Qiao Ling, Ramanujan RV, Zhu Jingchuan. Uncovering wear mechanism of a Fe2Ni2CrAl multi-principal elements alloy. J Mater Sci 2023;58:2660–75.

[28] Qiao Ling, Ramanujan RV, Zhu Jingchuan. Machine learning discovery of a new cobalt free multi-principal-element alloy with excellent mechanical properties. Mater Sci Eng, A 2022;Volume 845:143198.

[29] Qiao Ling, Zhu Jingchuan. Constitutive modeling of hot deformation behavior of AlCrFeNi multi-component alloy. Vacuum 2022;201:111059.

[30] Feng R, Zhang C, Gao Michael C, Pei Z, Zhang F, Chen Y, et al. High-throughput design of high-performance lightweight high-entropy alloys. Nat Commun 2021;12:4329.

[31] Li J, Fang Q, Liaw PK. Microstructures and properties of high-entropy materials: modeling, simulation, and experiments. Adv Eng Mater 2021;23:2001044.

[32] Wu Mingxu, Wang Shubin, Huang Haijun, Shu Da, Sun Baode. CALPHAD aided eutectic high-entropy alloy design. Mater Lett 2020;262:127175.

[33] Liu Feng, Xiao Xiangyou, Huang Lan, Tan Liming, Liu Yong. Design of NiCoCrAl eutectic high entropy alloys by combining machine learning with CALPHAD method. Mater Today Commun 2022;30:103172.

[34] Jiao Wenna, Li Tianxin, Chang Xiaoxue, Lu Yiping, Yin Guomao, Cao Zhiqiang, et al. A novel Co-free Al0.75CrFeNi eutectic high entropy alloy with superior mechanical properties. J Alloys Compd 2022;902:163814.

[35] Joseph Jithin, Stanford Nicole, Hodgson Peter, Fabijanic Daniel Mark. Understanding the mechanical behaviour and the large strength/ductility differences between FCC and BCC AlxCoCrFeNi high entropy alloys. J Alloys Compd 2017;726:885–95.

[36] Tang Zhi, Senkov Oleg N, Parish Chad M, Zhang Chuan, Zhang Fan, Santodonato Louis J, et al. Tensile ductility of an AlCoCrFeNi multi-phase high-entropy alloy through hot isostatic pressing (HIP) and homogenization. Mater Sci Eng, A 2015;647:229–40.

[37] Shi Quan-xin, Wang Cui-ju, Deng Kun-kun, Nie Kai-bo, Cao Miao, Gan Wei-min, et al. Work hardening and softening behavior of pure Mg influenced by Zn addition investigated via in-situ neutron diffraction. Mater Sci Eng, A 2020;772:138827.

[38] Li BS, Wang YP, Ren MX, Yang C, Fu HZ. Effects of Mn, Ti and V on the microstructure and properties of AlCrFeCoNiCu high entropy alloy. Mater Sci Eng, A 2008;498(Issues 1–2):482–6.

[39] Wang Zhaoqin, Wang Xiaorong, Yue Hui, Shi Guangtian, Wang Shunhua. Microstructure, thermodynamics and compressive properties of AlCoCrCuMn-x (x=Fe, Ti) high-entropy alloys. Mater Sci Eng, A 2015;627:391–8.

[40] Li A, Ma D, Zheng Q. Effect of Cr on microstructure and properties of a series of AlTiCr x FeCoNiCu high-entropy alloys. J Mater Eng Perform 2014;23:1197–203.

[41] Wang Xiao-Rong, Wang Zhao-Qin, Lin Tie-Song, He Peng. Microstructure, thermodynamics and compressive properties of AlCrCuNiZrx (x =0,1) high-entropy alloys. Mater Sci Technol 2016;32(12):1289–95.

[42] Tao-Tsung Shun, Chang Liang-Yi, Shiu Ming-Hua. Microstructures and mechanical properties of multiprincipal component CoCrFeNiTix alloys. Mater Sci Eng, A 2012;556:170–4.

[43] Wang XF, Zhang Y, Qiao Y, Chen GL. Novel microstructure and properties of multicomponent CoCrCuFeNiTix alloys. Intermetallics 2007;15(Issue 3):357–62.

[44] Zhang KB, Fu ZY, Zhang JY, Wang WM, Wang H, Wang YC, et al. Microstructure and mechanical properties of CoCrFeNiTiAlx high-entropy alloys. Mater Sci Eng, A 2009;508(Issues 1–2):214–9.

[45] Chen Yujie, Fang Yan, Fu Xiaoqian, Lu Yiping, Chen Sijing, Bei Hongbin, et al. Origin of strong solid solution strengthening in the CrCoNi-W medium entropy alloy. J Mater Sci Technol 2021;73:101–7.

[46] Sriharitha R, Murty BS, Kottada Ravi S. Alloying, thermal stability and strengthening in spark plasma sintered AlxCoCrCuFeNi high entropy alloys. J Alloys Compd 2014;583:419–26.

[47] Song RuoKang, Wei LiJun, Yang ChenXi, Wu SuJun. Phase formation and strengthening mechanisms in a dual-phase nanocrystalline CrMnFeVTi high-entropy alloy with ultrahigh hardness. J Alloys Compd 2018;744:552–60.

[48] Gao Xuzhou, Lu Yiping, Zhang Bo, Liang Ningning, Wu Guanzhong, Sha Gang, et al. Microstructural origins of high strength and high ductility in an AlCoCrFeNi2.1 eutectic high-entropy alloy. Acta Mater 2017;141:59–66.

[49] Wen H, Topping TD, Isheim D, Seidman DN, Lavernia EJ. Strengthening mechanisms in a high-strength bulk nanostructured Cu-Zn-Al alloy processed via cryomilling and spark plasma sintering. Acta Mater 2013;61:2769–82.

[50] Zhang Mengdi, Ma Yimo, Dong Wanqing, Liu Xingshuo, Lu Ye, Zhang Yifei, et al. Phase evolution, microstructure, and mechanical behaviors of the CrFeNiAlxTiy medium-entropy alloys. Mater Sci Eng, A 2020;771:138566.

[51] Moravcik Igor, Gouvea Larissa, Hornik Vit, Kovacova Zuzana, Kitzmantel Michael, Neubauer Erich, et al. Synergic strengthening by oxide and coherent precipitate dispersions in high-entropy alloy prepared by powder metallurgy. Scripta Mater 2018;157:24–9.

[52] Mote V, Purushotham Y, Dole B. Williamson-Hall analysis in estimation of lattice strain in nanometer-sized ZnO particles. J Theor Appl Phys 2012;6:6.